Physics of Fluids ARTICLE pubs.aip.org/aip/pof

Soliton groups and extreme wave occurrence in simulated directional sea waves

Cite as: Phys. Fluids **36**, 077101 (2024); doi: 10.1063/5.0213239
Submitted: 9 April 2024 · Accepted: 10 June 2024 ·
Published Online: 1 July 2024

View Online Export Citation CrossMark

A. V. Slunyaev[1,2,3,a)]

AFFILIATIONS

[1]HSE University, 25 Bolshaya Pechorskaya Street, Nizhny Novgorod 603950, Russia
[2]Institute of Applied Physics, RAS, 46 Ulyanov Street, Nizhny Novgorod 603950, Russia
[3]V.I. Il'ichev Pacific Oceanological Institute, FEB RAS, 43 Baltiyskaya Street, Vladivostok 690041, Russia

[a)]Author to whom correspondence should be addressed: slunyaev@ipfran.ru

ABSTRACT

The evolution of nonlinear wave groups that can be associated with long-lived soliton-type structures is analyzed, based on the data of numerical simulation of irregular deep-water gravity waves with spectra typical to the ocean and different directional spreading. A procedure of the windowed Inverse Scattering Transform, which reveals wave sequences related to envelope solitons of the nonlinear Schrödinger equation, is proposed and applied to the simulated two-dimensional surfaces. The soliton content of waves with different directional spreading is studied in order to estimate its dynamical role, including characteristic lifetimes. Statistical features of the solitonic part of the water surface are analyzed and compared with the wave field on average. It is shown that intense wave patterns that persist for tens of wave periods can emerge in stochastic fields of relatively long-crested waves. They correspond to regions of locally enhanced on average waves with reduced kurtosis. This eventually leads to realization of locally extreme wave conditions compared to the general background. Although intense soliton-like groups may be detected in short-crested irregular waves as well, they possess much shorter lateral sizes, quickly disperse, and do not influence the local statistical wave properties.

I. INTRODUCTION

Most frequently wind-generated oceanic gravity waves and swells are treated as linear combinations of random harmonic or Stokes waves with independent individual phases. Nonlinear effects are considered by theories to be weak corrections unless waves start to break. Due to the specific property of the deep-water dispersion relation, the second-order quadratic nonlinearity corresponds to non-resonant wave triplets, thus manifests itself solely through alteration of individual wave shapes from sinusoidal. In the spectral Fourier representation, this effect is described by phase-locked bound harmonics.[1,2]

Exact resonances are allowed between deep-water gravity waves in the next-order cubic nonlinearity. Within the traditional phase-averaged kinematic theory on the evolution of the wave spectral density, the four-wave interactions govern an extremely slow evolution of the wave spectrum with the characteristic timescale inverse proportional to the wave steepness in power four.[2]

The keen interest in a couple of recent decades to quasi-resonant wave quartet interactions that support the dominant type of deep-water wave instability caused by the Benjamin–Feir mechanism (the modulational instability) has resulted in the general recognition of this phenomenon to be an effective mechanism of water wave intensification. In addition to the acceptance by a part of the scientific community of the hypothesis that registered rogue waves (abnormally high waves, see, e.g., Ref. 3) are predominantly caused by the Benjamin–Feir instability,[4,5] it has been proven theoretically and experimentally that the probability of occurrence of high waves increases under the conditions of developing modulational instability.[6–11] The corresponding wave dynamics occurs with a sub-kinetic timescale inverse proportional to the squared wave steepness. Thus, the related effects can represent a serious threat in the ocean, which cannot be predicted by the existing forecasting routines.[12] Meanwhile, we should mention that this viewpoint remains still disputable due to some works, claiming that the modulational instability conditions are not achievable in the real ocean, see, e.g., Refs. 13–16.

The instability analysis of a plane wave with respect to long perturbations is today a classic exercise, see, e.g., Ref. 17. The instability threshold relates the wave steepness and the length of perturbation. The nonlinear stage of the Benjamin–Feir instability may be effectively described within the weakly nonlinear equation for slow modulations, the nonlinear Schrödinger equation (NLSE), in terms of so-called breather solutions.[18–20] While breathers represent idealized examples of wave trains, other configurations of unstable nonlinear wave sequences admit exact analysis within the NLSE too (see, e.g., Ref. 12). The general description of the nonlinear stage of the modulational instability within the NLSE is, in principle, possible, thanks to integrability of this equation by the Inverse Scattering Transform[19,20] (IST), but it is very difficult technically. Importantly, the model solutions for modulationally unstable waves are frequently considered as theoretical prototypes of rogue waves. Many of them have been successfully reproduced in laboratory conditions, where they retain similarity to the NLSE solutions even in strongly nonlinear and strongly dispersive regimes.[21–26]

From the viewpoint of the IST, a breather solution of the NLSE is an envelope soliton on a pedestal formed by the background plane wave (see, e.g., the book by Akhmediev and Ankiewicz[27] or the discussion in Ref. 28). All modulationally unstable modes are linked to discrete eigenvalues of the scattering problem associated with the NLSE;[19,20] the eigenvalues under the decaying boundary conditions in infinite line correspond to envelope solitons and specify their amplitudes and velocities. It was shown in Ref. 28 that the inherent amplitude of a breather is exactly the same as the amplitude of the envelope soliton when the breather background is removed. The distinction between solitons and breathers in irregular wave fields (see, e.g., Ref. 29) may be quantified in terms of the ratio between the soliton/breather amplitude and the characteristic amplitude of the background. In particular, the expression for Kuznetsov breather reduces to an envelope soliton in the limit of negligibly small background waves; the Peregrine breather is characterized by a soliton with twice larger amplitude than the unperturbed background.[3,28]

Therefore, for a meaningful interpretation of nonlinear wave fields, it seems to be convenient to operate with characteristics of envelope solitons, which are the base elements of coherent wave dynamics. Envelope solitons, including the limit of short groups of steep waves, were registered in numerical and also laboratory simulations, see the bibliographic review in our preceding paper Ref. 30 and references therein, which we do not reproduce here. More recently, the applicability of the envelope soliton concept to describe interacting sequences of nonlinear wave groups ("soliton gases") was shown in numerical and laboratory experiments;[31] an emergence of envelope solitons from irregular waves in numerical experiments was discussed in Ref. 32; IST-based perturbation theory was applied in Ref. 33 to interpret the dynamics of coupled envelope solitons modeled numerically. A measurement of a giant wave group in the Atlantic Ocean associated with an NLSE envelope soliton was reported in Ref. 34. A greater number of wave groups recorded in the Pacific Ocean, treated as envelope solitons, were analyzed in the recent Ref. 35.

Crucially, in the majority of conducted studies, the interpretation of propagating waves in terms of envelope solitons (or breathers) was performed at a single spatial location. It remained unclear whether the identified envelope solitons behaved similar to solitons at a later time. In particular, where is the registered "envelope solitons" long-lived structures? According to the recent experimental and numerical data,[30,33,35–38] intense envelope solitons of collinear waves can, indeed, survive for $O(10^1–10^2)$ wave periods and more in calm water, and also when surrounded by irregular background waves and when interact with other envelope solitons.

Note that though the results of the one-dimensional NLSE theory may be extended to oblique perturbations[39] and opposite (standing) wave systems,[26] in the general situation of essentially directional waves, the qualitative picture of the nonlinear surface wave dynamics and the corresponding approximate solutions within the two-dimensional NLSE change dramatically. The 2D version of the NLSE losses the property of integrability; the nonlinearity becomes defocusing in the lateral direction; planar envelope solitons are transversely unstable; stable configurations of solitary patterns of directional waves in deep water are unknown. The effect of modulational instability quickly vanishes when the directional spreading increases[8,40] and may be efficient only under specific conditions, e.g., of waves guided by topographic or current peculiarities.[41–43]

Thus, though some evidences of long-term propagation of coherent nonlinear groups of unidirectional waves in deep water are present in the literature, it is until now completely unclear how long they can exist under the conditions of directional waves natural to the open ocean. The present work addresses this question by means of the direct numerical simulation of nonlinear evolution of irregular directional surface waves within the primitive hydrodynamic equations, and subsequent analysis of the envelope soliton content in the simulated surfaces using a windowed IST (WIST)-based procedure.

The paper is organized as follows. In order to increase the chance to face a large-amplitude envelope soliton in the stochastic field of water waves, we use a *particular realization* of *random* JONSWAP *waves* from Ref. 44, which, in the planar geometry, leads to the formation of a long-lived intense envelope soliton.[30] The approach, which we follow to produce the initial conditions for the simulation of directional waves with a given width of the angular spectrum, is described in Sec. II. The main features of the conducted direct numerical simulations are given in Sec. III. The windowed IST procedure (called hereafter WIST), which was presented in Ref. 30 for unidirectional waves, is generalized in the present work to the case of directional waves as described in Sec. IV. The immediate result of its application to the simulated data is presented in Sec. IV as well. A deeper analysis of the soliton content in the simulated wave surfaces, including the estimation of the characteristic lifetimes of envelope solitons in fields with different directional spreading, is performed in Sec. V. The impact of soliton-like wave patterns on the statistical properties of water waves is evaluated in Sec. VI. The main conclusions of the work are summarized in Sec. VII.

II. CONSTRUCTION OF THE INITIAL CONDITIONS

We proceed from the expectation that the probability of formation of a long-lived soliton-type group in the field of irregular broadbanded sea waves is low. In this work, specific initial conditions for the numerical simulation of directional gravity waves are constructed, such that in the limit of a vanishing directional spread, the modeling replicates the simulation of unidirectional waves where a long-lived group was, indeed, observed. Such an event in the field of collinear waves was analyzed in detail in Ref. 30; it corresponds to the realization No. 295 from the stochastic simulations reported in Ref. 44. Few other realizations from that set were shown to contain long-lived soliton-type groups too.[30] Thus, the considered realization is specific but not unique.

We take that particular realization of irregular waves No. 295 as the base, $\eta_b(x) = \eta_{295}(x, t = 0)$, and produce two-dimensional fields of the surface displacement, $\eta(x, y, t = 0)$ with $\eta(x, y = 0, t = 0) = \eta_b(x)$, following the method described later. Here, η denotes the water surface displacement, x and y are the spatial coordinates along and transverse the main direction of wave propagation, and t is the time.

The initial condition $\eta_{295}(x, t=0)$ corresponds to the JONSWAP frequency spectrum $S(\omega)$ with the peak period $T_p = 10$ s and the peakedness parameter $\gamma = 3$, which is transformed to the wavenumber spectrum $S(k)$ according to the linear dispersion relation for deep-water waves,

$$k = \frac{\omega^2}{g}, \tag{1}$$

and then to Fourier amplitudes for wavenumbers k, $|\hat{\eta}_b(k)| = S(k)$, where the "hat" stands for the Fourier transform function. Here, ω denotes the cyclic frequency and $g = 9.81$ m/s^2 is the acceleration due to gravity. Correspondingly, the peak wavenumber is $k_p \approx 0.04$ rad/m (the dominant wavelength is about 150 m). The nominal significant wave height H_s, which is about four times the root mean square surface displacement η_{rms}, is $H_s \approx 4\eta_{rms} \approx 3.5$ m, see details in Ref. 44.

At first, a trial (tentative) irregular surface wave field $\eta_{tr}(x, y)$ is produced, which is characterized by the same distribution of energy in the Fourier transform for wavenumbers as the base wave, $|\hat{\eta}_{tr}(k)| = S(k)$, where k is now the length of wave vectors, $k = |\mathbf{k}|$, $\mathbf{k} = (k_x, k_y)$, for the two-dimensional surface $\eta_{tr}(x, y)$. The directional distribution, $|\hat{\eta}_{tr}(k_x, k_y)| = S(k)D(\theta)$, is defined according to the popular in oceanography cosine-squared function, same as in Ref. 45,

$$D(\theta) = \begin{cases} \dfrac{2}{\Delta\theta} \cos^2 \dfrac{\pi\theta}{\Delta\theta} & \text{if} \quad |\theta| \le \dfrac{\Delta\theta}{2}, \\ 0 & \text{if} \quad |\theta| > \dfrac{\Delta\theta}{2}, \end{cases} \tag{2}$$

where θ is the angle with respect to the Ox axis, $\tan\theta = \frac{k_x}{k_y}$, and the parameter $\Delta\theta$, $0 \le \Delta\theta \le 180°$, determines the sector of possible wave directions with respect to the dominant direction $\theta = 0$. Complex phases of the Fourier transform $\hat{\eta}_{tr}(k_x, k_y)$ are set to be random and uniformly distributed.

In order to introduce an additional degree of randomness, each amplitude of the Fourier transform for the 2D trial initial condition $|\hat{\eta}_{tr}(k_x, k_y)|$ was multiplied by a normally distributed random factor. As a result, the Fourier amplitudes $\hat{\eta}_{tr}(k_x, k_y)$ are irregular in both complex phases and amplitudes. The distribution for wavenumbers corresponds well to the JONSWAP function $S(k)$; the distribution of wave propagation directions is described on average by the $\cos^2$ shape (2).

At the next step, the residual wave shape for $y = 0$ between the base and the trial waves is computed, $\Delta_{1D}(x) = \eta_b(x) - \eta_{tr}(x, y=0)$; it is transformed to a two-dimensional field $\Delta_{2D}(x, y)$ by introducing the directional distribution specified by the function $D(\theta)$ with the same choice of $\Delta\theta$, so that the distribution for the wave vector lengths retains, $\hat{\Delta}_{1D}(k) = \hat{\Delta}_{2D}(k)$. The generated field $\Delta_{2D}(x, y)$ is then superimposed with the trial field, $\eta(x, y, 0) = \eta_{tr}(x, y) + \Delta_{2D}(x, y)$, what gives the desired initial condition $\eta(x, y, 0)$ with the property $\eta(x, 0, 0) = \eta_b(x)$. Since the correction function $\Delta_{2D}(x, y)$ is characterized by the same distribution of energy between wave lengths and directions as the irregular part, the resultant wave surface keeps the distributions unchanged, i.e., the surface $\eta(x, y, 0)$ corresponds to JONSWAP waves with the given directional spread $\Delta\theta$.

Examples of the generated water surfaces for different directional spreads $\Delta\theta$ are shown in Fig. 1. The surface has the size $L_x \approx 9600$ m $\times$ $L_y \approx 2400$ m, which is about 23 square kilometers. The domains are periodic in both directions Ox and Oy. The longitudinal sections at $y = 0$ are shown with red color; they represent identical wave shapes $\eta_b(x)$.

Finally, the surface velocity potential at the initial moment of time, $\Phi(x, y, t=0)$, is computed based on the generated surface displacement $\eta(x, y, 0)$ according to the linear theory.[17] These fields are used to initiate the direct numerical simulations as detailed in Sec. III.

Five realizations per each value of the spreading parameter $\Delta\theta$ from the set $\Delta\theta = \{12°, 24°, 36°, 48°, 62°\}$ have been simulated in this study. The range of directional spreads is taken similar to Ref. 45. One may see from Fig. 1 that the simulated conditions correspond to ones from long-crested, $\Delta\theta = 12°$, to pretty short-crested, $\Delta\theta = 62°$. The upper panel in Fig. 1 corresponds to the planar case $\Delta\theta = 0$, which is used in this work for the reference. All the realizations are characterized by the significant wave height $H_s \approx 3.5$ m.

III. NUMERICAL SIMULATION OF DIRECTIONAL WAVES

In this work, the evolution of gravity waves on the surface of infinitely deep water is simulated using the primitive equations of hydrodynamics for potential motions of the ideal fluid.[17] The governing system of equations consists of two-surface boundary conditions:

$$\eta_t + \nabla\Phi \cdot \nabla\eta = \varphi_z\left(1 + \nabla\eta^2\right) \quad \text{at} \quad z = \eta, \tag{3a}$$

$$\Phi_t + g\eta + \frac{1}{2}(\nabla\Phi)^2 = \frac{1}{2}\varphi_z^2\left(1 + \nabla\eta^2\right) \quad \text{at} \quad z = \eta, \tag{3b}$$

the Laplace equation

$$\nabla^2\varphi + \varphi_{zz} = 0 \quad \text{for} \quad z \le \eta, \tag{4}$$

and the decaying at infinity bottom condition

$$\varphi \to 0 \quad \text{when} \quad z \to -\infty. \tag{5}$$

Here, $\varphi(x, y, z, t)$ is the velocity potential, and $\Phi(x, y, t) = \varphi(x, y, z = \eta, t)$. The gradient operator acts in the horizontal plane (x, y) only, $\nabla \equiv (\partial/\partial x, \partial/\partial y)$; the axis Oz is upward directed. The set of Eqs. (3)–(5) for the initial conditions $\eta(x, y, 0)$ and $\Phi(x, y, 0)$ constitutes the Cauchy problem in a closed form, which is solved numerically using the High-Order Spectral Method[46] (HOSM), see details of realization of the algorithm in Refs. 47 and 48.

In the HOSM, the velocity field in the perturbed upper water layer is approximated using the Taylor expansion of the order M near the horizon $z = 0$, what allows to relate the surface velocity potential $\Phi(x, y, t)$ with the potential at the water rest level $\varphi(x, y, z=0, t)$, in order to use the analytic solution to the Laplace equation. Therefore, the method is fully accounting dispersive effects, but is limited in nonlinearity. For the choice $M = 3$ which is used in the present work, it describes accurately the nonlinear interactions between up to 4 waves, what, in particular, allows simulation of the Benjamin–Feir instability and envelope solitons. Few simulations with a higher nonlinear parameter $M = 4$ were also performed but did not show any significant difference.

Following the approach by Dommermuth,[49] the nonlinear terms of simulated Eq. (3) were put in force slowly for the first

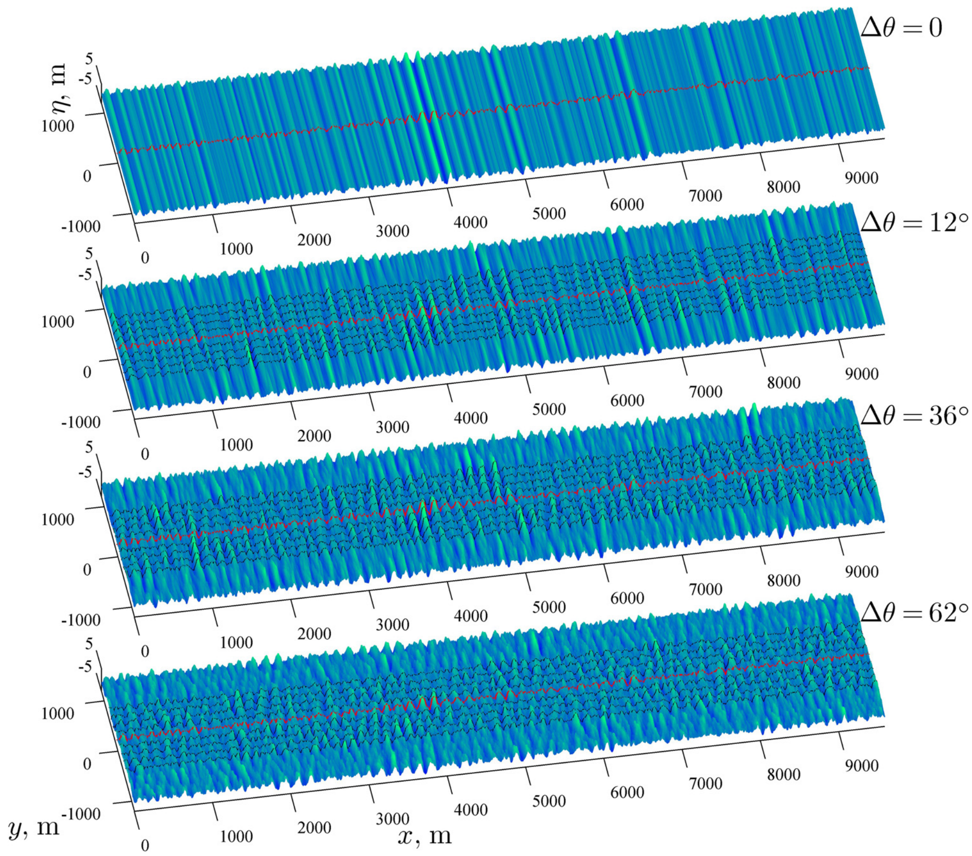

FIG. 1. Examples of initial surfaces $\eta(x, y, 0)$ characterized by different wave direction spreads $\Delta\theta$. The longitudinal sections at $y = 0$ are shown with the red color. Other longitudinal sections used in the windowed IST analysis are shown with the black color.

$20T_p$ ($0 \le t \le 200$ s) to ensure adiabatic transition of the linear initial condition to nonlinear waves.

The numerical integration in time was performed using the 4-th order Runge–Kutta method with the constant step of 0.0625 s. The accuracy of simulations was controlled by checking the conservation of the total mechanical energy. In all simulations, the relative deviation of the total energy in the periods of truly nonlinear simulations 200 s $\le t \le$ 1400 s was within the range -7.8×10^{-5} and $+7.5 \times 10^{-4}$. Wave overturning did not occur in these simulations.

IV. SEARCH FOR ENVELOPE SOLITONS

The simulated water surfaces are further analyzed to reveal wave patterns similar to envelope solitons of the nonlinear Schrödinger equation. The NLSE is the weakly nonlinear approximation for waves with narrow spectrum. For deep-water waves propagating mainly along the Ox axis, the equation may be written in the following form:[17]

$$i\left(\frac{\partial\psi}{\partial t} + C_0\frac{\partial\psi}{\partial x}\right) + \frac{\omega_0 k_0^2}{2}|\psi|^2\psi + \frac{\omega_0}{8k_0^2}\frac{\partial^2\psi}{\partial x^2} - \frac{\omega_0}{4k_0^2}\frac{\partial^2\psi}{\partial y^2} = 0, \quad (6)$$

where k_0 and ω_0 are the carrier wavenumber and frequency related by the dispersion relation (1), respectively, $C_0 = \omega_0/2/k_0$ is the group velocity of the carrier wave, and $\psi(x, y, t)$ is the complex wave amplitude so that the surface displacement to the leading order reads

$$\eta(x, y, t) = \frac{1}{2}\psi(x, y, t)\exp(i\omega_0 t - ik_0 x) + c.c. \quad (7)$$

Waves propagate mainly along the Ox axis. As the linear part of the NLSE (6) corresponds to the Taylor expansion of the dispersion relation $\omega(\mathbf{k}) = \sqrt{gk}$ in the close vicinity of the carrier wave $\mathbf{k}_0 = (k_0, 0)$, namely, $(\omega - \omega_0) \approx \frac{\partial\omega}{\partial k_x}|_{\mathbf{k}_0}(k_x - k_0) + \frac{1}{2}\frac{\partial^2\omega}{\partial k_x^2}|_{\mathbf{k}_0}(k_x - k_0)^2 + \frac{1}{2}\frac{\partial^2\omega}{\partial k_y^2}|_{\mathbf{k}_0}k_y^2$, it can be easily seen that the dispersion coefficients in (6) have different signs. The effect of transverse dimension enters the two-dimensional NLSE (6) solely through the last term. If this term is canceled, the theories (6) and (7) describe a strictly planar problem. In this case, the NLSE possesses the property of integrability by means of the IST,[19,20] which allows a comprehensive analysis of complicated nonlinear wave phenomena using appropriate mathematical methods.

In particular, envelope solitons that have the form of stable groups are exact solutions of the integrable NLSE. These groups do not disperse with time and interact elastically with all other waves including envelope solitons. One envelope soliton of the one-dimensional NLSE is given by the exact solution,

$$\psi_{ES}(x,t) = A_s \frac{\exp\left[\frac{i}{4}s^2\omega_0 t + i\phi_s\right]}{\cosh[\sqrt{2}sk_0(x - x_s - C_0 t)]}, \quad s = k_0 A_s, \tag{8}$$

where A_s is the soliton amplitude; the maximum wave steepness s has the meaning of the dimensionless amplitude and characterizes the degree of wave nonlinearity. The parameters x_s and ϕ_s are the reference location and phase, respectively. The soliton (8) propagates with the group speed of the carrier C_0 and consists of individual waves of the length of the carrier. Their apparent frequency $\omega_0\left(1+\frac{1}{4}s^2\right)$ experiences nonlinear upshift. The solution (8) may be generalized using the Galilean transformation, and then envelope solitons may have wavenumber correction k_s and corresponding correction to the group velocity, V_s, and also to the frequency; we omit these details here, and they may be found in Ref. 50. An exact solution of the two-dimensional NLSE (6) in the form of a planar envelope soliton may be straightforwardly constructed from (8), though it is known to be unstable with respect to sufficiently long transverse perturbations.[51]

It is clear from (8) and (7) that higher envelope solitons contain smaller number of wave oscillations. The soliton groups are shown in Fig. 2 for a relevant range of the steepness parameter. Note that even steeper and shorter envelope solitons than shown here were reproduced in laboratory experiments.[36] The characteristic spatial width w of an envelope soliton (8) may be defined as

$$w(A_s, k_0) = \frac{W}{sk_0}, \tag{9}$$

where W is a constant. The blue and red curves in Fig. 2 show the bands $\pm w$ for the choices $W = 2$ and $W = 5$, respectively, which will be used later in order to select spatial areas occupied by solitons.

The principle information about coherent wave structures such as solitons or breathers at any given instant t_0 is contained in the

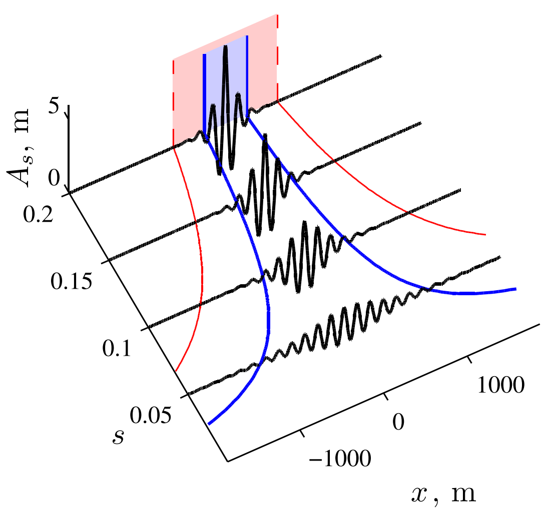

FIG. 2. Surface displacements $\eta(x, 0)$ that correspond to envelope solitons (7) and (8) with $k_0 = 0.04$ rad/m, $x_s = 0$, and $\phi_s = 0$ (black curves) for the steepness parameter $s = \{0.05, 0.1, 0.15, 0.2\}$. The blue and red curves show the bands $\pm w$ (9) with $W = 2$ and $W = 5$, respectively.

discrete spectrum $\{\lambda\}$ of so-called associated (with the NLSE) scattering problem,[19,52] which has the form of an eigenvalue problem on the column vector function $\Psi(x)$,

$$\frac{d}{dx}\Psi = \sqrt{2}k_0 \begin{pmatrix} \lambda & k_0\psi(x,t_0) \\ -k_0\psi^*(x,t_0) & -\lambda \end{pmatrix} \Psi. \tag{10}$$

When decaying boundary conditions are imposed, $\Psi(x \to \pm\infty) \to 0$, then each discrete eigenvalue λ corresponds to one envelope soliton with the amplitude A_s and velocity V_s, which are specified by the following relation:

$$\lambda = \frac{1}{2}k_0 A_s + \frac{i}{\sqrt{2}}\frac{V_s - C_0}{C_0}. \tag{11}$$

Here, the soliton velocity V_s is assumed to be related to the intrinsic soliton wavenumber k_s through the linear relation for a wave group velocity $V_s = \frac{1}{2}\sqrt{\frac{g}{k_s}}$.

All solitons (and breathers) if they are present in the wave field of arbitrary complexity but governed by the integrable NLSE may be found using the direct scattering problem (10), though the implementation of this procedure is technically demanding, see, e.g., Refs. 53 and 54.

A procedure of the windowed IST (WIST) analysis was proposed in our works Refs. 28 and 55 and further improved in Refs. 30 and 50, where its ability to relatively accurately estimate the amplitudes A_s, velocities V_s, and locations x_s of solitons in broadband fields of unidirectional intense waves was demonstrated. The following key characteristics of the WIST approach may be emphasized:[30] (i) the approach is targeted to the search of intense solitons; (ii) a windowed transform is used to identify approximate locations of envelope solitons; the information about their complex phases is not available; (iii) the wave envelope is reconstructed from the surface displacement using the high-order Dysthe theory for bound waves, and the relation (7) is just the first-order approximation; (iv) at the second stage, the direct scattering problem is solved in a larger sampling window to estimate the soliton parameters A_s and V_s more precisely.

In order to apply the WIST to two-dimensional fields of directional waves, the simulated wave surfaces $\eta(x, y, t)$ have been sliced into longitudinal sections at a number of transverse locations $y = d_n$, $d_n = \{0, \pm 150, \pm 300, \pm 450, \text{and } \pm 600\,\text{m}\}$, as shown by colored curves in Fig. 1. This spacing roughly corresponds to one wavelength. As the soliton group is expected to emerge near the middle section $y = 0$, we focus primarily on the region close to it.

The sequences of spatial series $\eta(x, d_n, t_m)$ for all slices d_n and time instants t_m with the stepping $t_{m+1} - t_m = T_p/2 = 5$ s have been analyzed one-by-one using exactly the same WIST method as in Ref. 30. The WIST procedure returns the set of soliton parameters $\{(A_s, V_s, x_s)\}$ for each space series. If more than one envelope soliton is detected for approximately the same location, only the one with the larger amplitude is taken for consideration. The result of this analysis is shown for two spreads $\Delta\theta$ in Figs. 3 and 4. There, the amplitudes of revealed solitons in different longitudinal slices for the time instants $t = 0, 10, \ldots, 2800$ s are shown with circles. The size and color of the circles reflect values of the soliton amplitudes A_s.

In both cases presented in Fig. 3, intense envelope solitons with amplitudes up to about $A_s \approx 3.5$ m are found. The total number of soliton-like groups found by the WIST per each choice of the directional spreading parameter $\Delta\theta$ is of the order 1×10^4 (this estimate

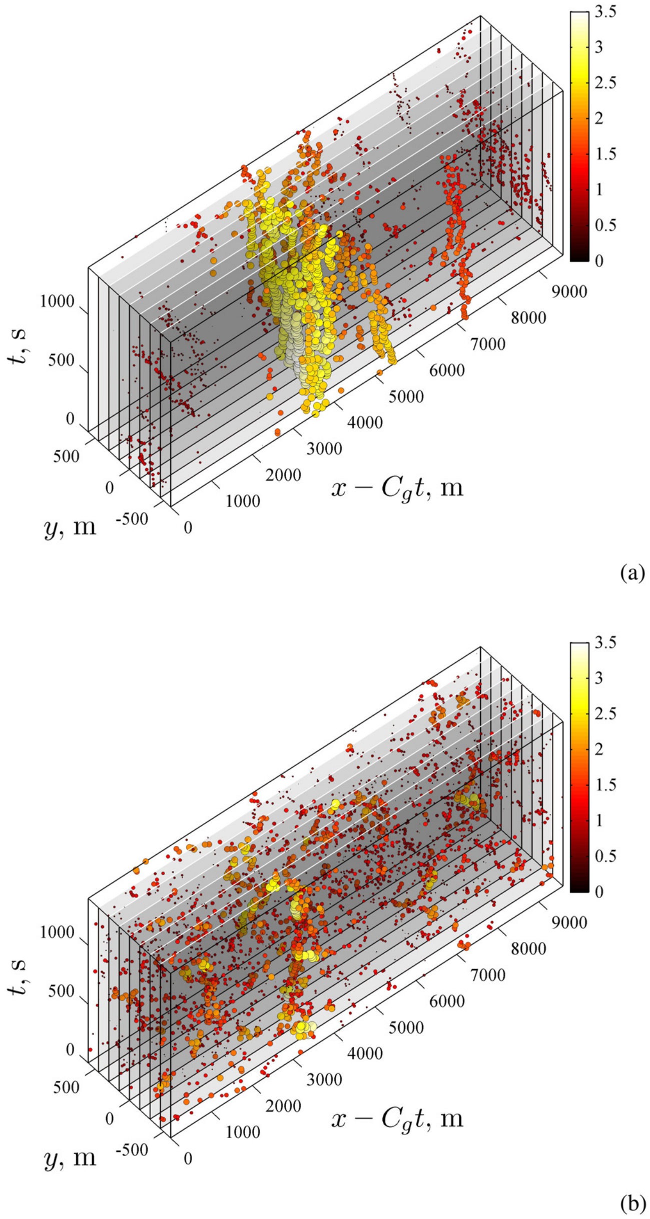

FIG. 3. Distribution of soliton amplitudes A_s (circles) found using the WIST applied to longitudinal cuts (shaded planes) of the water surfaces for two simulations with $\Delta\theta = 12^\circ$ (a) and $\Delta\theta = 62^\circ$ (b). Size and color of the circles reflect the magnitudes of soliton amplitudes, see the colorbar.

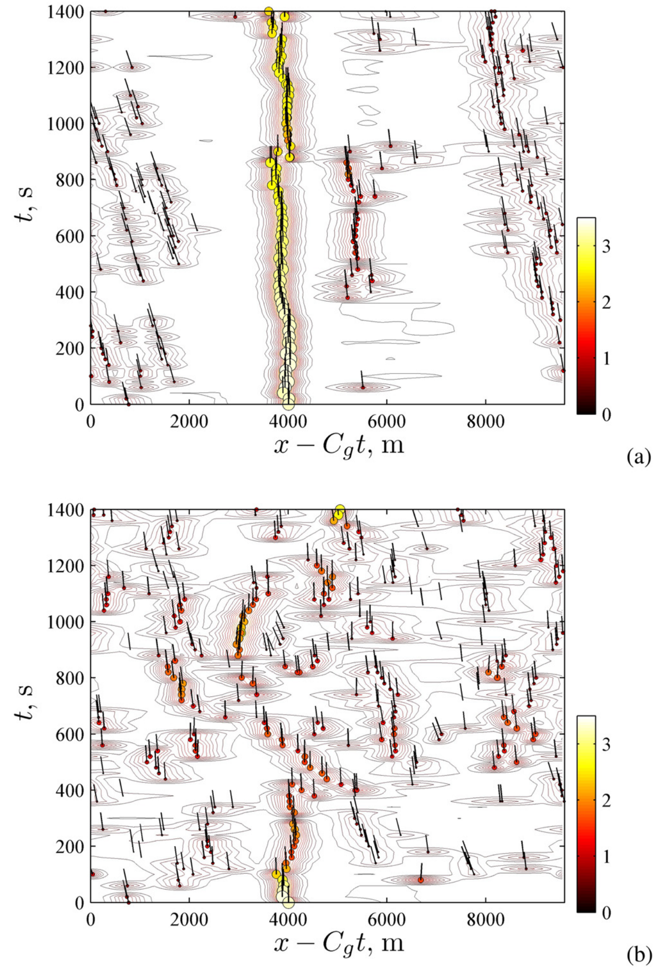

FIG. 4. Soliton amplitudes shown in Figs. 3(a) and 3(b) for the slice $y = 0$ (circles) and forecasts of the soliton tracks within next 1 min (sticks). Level lines correspond to the amplitude function $A(x, 0, t)$.

counts one soliton group revealed at two different time moments or two different lateral positions as two). The number of revealed solitons per each instant does not approximately change with time. Meanwhile, a remarkable difference between the two examples given in Fig. 3 is obvious. In the long-crested wave field [Fig. 3(a)], large soliton amplitudes are located laterally close to each other. They almost do not move in the system of references traveling with the dominant wave propagation velocity determined as $\mathbf{C}_g = (C_g, 0)$, $C_g = \omega_p/(2k_p) \approx 7.8$ m/s. The situation of short-crested waves [Fig. 3(b)] is characterized by a great extent random arrangement of detected small-amplitude solitons in the space-time domain; large-amplitude solitons (large bright spots) appear for short time intervals.

The impression of a greater number of small-amplitude solitons in the case of a broader angular spectrum is rather misleading. Distributions of detected soliton amplitudes for different values of the parameter $\Delta\theta$ are shown in Fig. 5; at first glance, they are rather similar. In particular, 45%–60% of soliton amplitudes A_s are less than 1 m, and only 15%–25% of them are above $H_s/2$. (Envelope solitons with very small amplitudes were discarded by the WIST procedure.) It is important for the present study that the distributions for smaller values of $\Delta\theta$ are characterized by slightly increased fractions of solitons with large amplitudes, which may be noticed in Fig. 5.

A further analysis is presented in Fig. 4, where the same distribution of soliton amplitudes as in Fig. 3 is given by color circles for a single longitudinal cut $y = 0$. These data are also used to build a soliton amplitude function $A(x, y, t)$ as will be described in Sec. V, which is

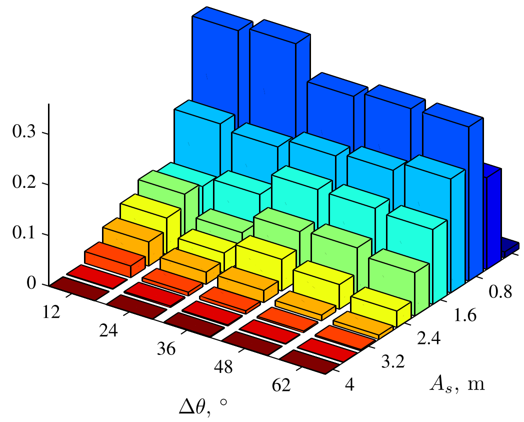

FIG. 5. Distributions of revealed soliton amplitudes for different widths of the angular spectrum $\Delta\theta$ (each case contains between 1.2×10^4 and 1.41×10^4 amplitudes).

represented by contour curves. In addition, the estimated soliton velocities V_s are used to make predictions of future soliton positions. In the figure, the expected tracks of solitons in the next 60 s are shown with black line segments. Note that the graphs are presented in the system of references moving with the group velocity $C_g \approx 7.8$ m/s; the values of V_s range from 5.3 to 8.2 m/s.

It is obvious from Fig. 4(a) that the path of the maximum soliton, which is originally located at $x_0 \approx 4000$ m is traced correctly except for the time $t \approx 900$ s when, for some reason, the position of the soliton quickly shifts by about 250 m (which is below the estimated soliton length, see Fig. 2). It is also clear that the estimated velocities of smaller-amplitude solitons well agree with their actual movements; many of them travel with speeds smaller than C_g.

The picture in Fig. 4(b) is much less regular; the estimated velocities seem to better characterize the apparent motion of solitons, which have large amplitudes. Note that here we completely disregard the velocity components transverse to the main direction of wave propagation; therefore, it is naturally to expect that the conditions of short-crested waves should be described less consistently.

V. INVESTIGATION OF SOLITON-LIKE WAVE GROUPS

In the reference simulation[30] of planar waves $\Delta\theta = 0$, an intense envelope soliton emerged and stably propagated for more than two hundred wave periods with velocity very close to dominant waves, $V_s/C_g = 1.00 \pm 0.02$, and approximately constant amplitude, $A_s/(4\eta_{rms}) = 1.00 \pm 0.16$. Let us consider the effect of directional wave propagation on this soliton. In the limit $\Delta\theta \to 0$, the soliton structure is located at $t = 0$ near $x_0 = 4000$ m and $y_0 = 0$, see Fig. 3(a). To select the area in the vicinity of the soliton, we use a comoving mask of a round shape,

$$(x - x_0 - C_g t)^2 + (y - y_0)^2 \le w^2, \tag{12}$$

as shown in Figs. 6 and 7 by dashed green lines. Here, w is given by (9), where we use the peak wavenumber, $k_0 = k_p$, the steepness $s = 0.14$, which corresponds to the envelope soliton with amplitude equal to the significant wave height, $A_s = 4\eta_{rms} \approx 3.5$ m, and $W = 5$, see red curves in Fig. 2.

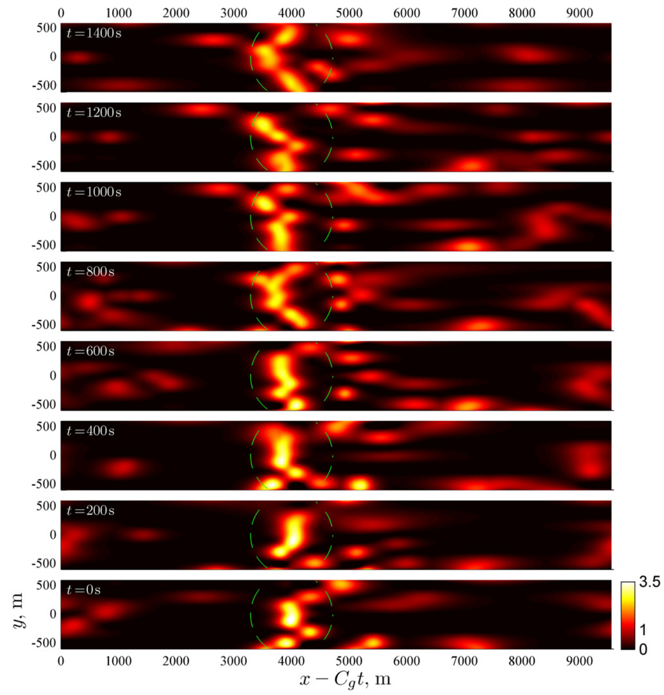

FIG. 6. Soliton fields $A(x, y, t)$ (13) found by the WIST procedure at different instants of time for a simulation with $\Delta\theta = 12°$. The pseudocolor gives the values of A in meters, see the colorbar. The region (12) with $x_0 = 4000$ m and $y_0 = 0$, $w \approx 880$ m is shown by the dashed green contour.

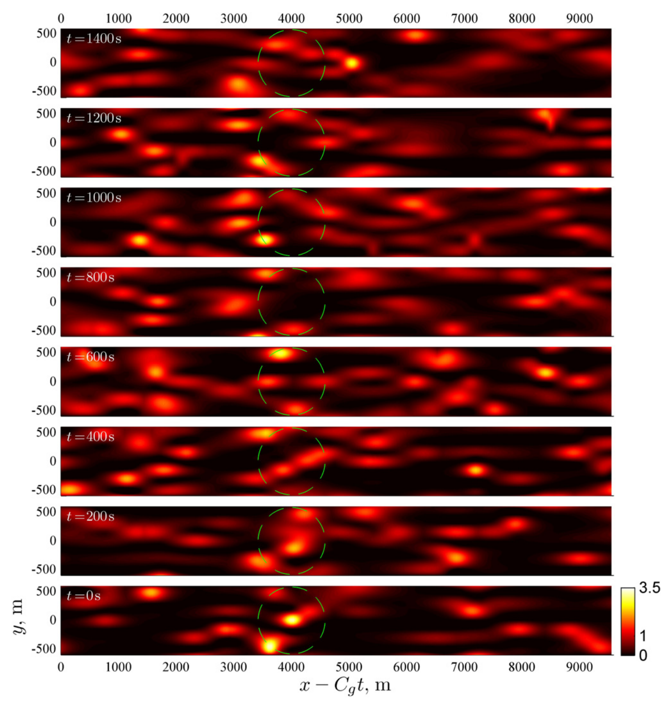

FIG. 7. Same as in Fig. 6 but for a simulation with $\Delta\theta = 62°$.

In Figs. 6 and 7, the pseudocolor represents the combined soliton function $A(x, y, t)$, which is constructed as the maximum envelope over all revealed solitons with the parameters $\{(A_s, k_s, x_s)\}$ obtained by the WIST. The function $A(x, y, t)$ is first defined on a sparse grid $y = \{d_n\}$ and $t = \{t_m\}$ where the WIST is performed,

$$A(x, y = d_n, t = t_m) = \max_s |\psi_{ES}(x, 0; A_s, k_s, x_s)|, \quad (13)$$

and then interpolated onto a finer grid to produce smooth patterns. Isolevels of this function are shown in Fig. 4.

Eight panels in Figs. 6 and 7 correspond to different time instants of the wave field evolution. Note that the transverse size of the soliton fields $A(x, y, t)$, 1200 m, is about twice smaller than L_y; the fields $A(x, y, t)$ are periodic along the longitudinal axis Ox but are not periodic in the transverse direction.

It is clear from Fig. 6 that a long-lived wave pattern, which is recognized by the WIST as an intense envelope soliton, is, indeed, generated in the selected area and retains significant energy throughout the simulation period. The intense soliton-type structure is already detected at $t = 0$. It is interesting to note that the transverse shape of the soliton pattern exhibits significant transformation over time, and it may be oriented transverse or oblique to the main wave course, although the pattern is still recognized as containing a soliton. The revealed soliton-like structure has the transverse size greater than that in the direction of propagation, but it never extends to the entire available transverse size.

Another stable structure of a smaller-amplitude may be also found in Fig. 6 at $x - C_g t \approx 7000$ m, $y \approx -500$ m in the time interval from $t = 0$ to $t = 1200$ s. Some more patterns that correspond to wave groups recognized as envelope solitons may be seen in Fig. 6 as well, but they survive for significantly shorter periods of time.

The picture of the soliton field $A(x, y, t)$ in short-crested waves looks very different, see Fig. 7. A bright spot in the center of the selected domain at $t = 0$ becomes much less pronounced at $t = 200$ s when the simulation becomes truly nonlinear and vanishes after. At later times, new energetic spots appear at different instants and in different places, which correspond to wave groups recognized by the WIST as intense NLSE solitons, though they quickly disappear. The revealed "envelope solitons" in the short-crested sea state have transverse sizes similar to the longitudinal ones. Comparing Fig. 7 against Fig. 6, one may conclude that the number of soliton-like patterns is greater in the short-crested case.

Assuming that the selected according to condition (12) area in Fig. 6 at all times captures the soliton of our interest, we estimate its instantaneous amplitude as the maximum of the soliton function $A(x, y, t)$ in this region. We do so for all five simulated realizations that correspond to $\Delta\theta = 12°$ and also for the other conditions of the directional spreading. The results of this processing are presented in Fig. 8. The soliton amplitudes in the selected regions are shown by black curves for each realization. In addition, the shaded areas show the maximum soliton amplitudes in the entire domain of simulation among all realizations. In the leftmost panel for $\Delta\theta = 12°$, the maximum soliton amplitudes found in the simulation of unidirectional waves[30] are also given by blue dots.

It follows from Fig. 8 that in all the wave realizations, intense soliton-like groups are found initially close to the point (x_0, y_0) with amplitudes in the range $3.2 - 4$ m. The intense soliton-like groups decay with time in all simulations of directional waves, unlike in the simulation of strictly planar waves. The evolution of soliton amplitudes is generally synchronous in all experiments with long-crested waves $\Delta\theta = 12°$. In cases of intermediate directional spreads $\Delta\theta = 24°$ and $\Delta\theta = 36°$, the initial soliton amplitudes in different realizations can differ considerably and can exceed the value of H_s; the subsequent evolution of the amplitudes can also be quite different. Under conditions of relatively narrow angular spectrum $\Delta\theta \leq 36°$, the highest solitons occur in the selected region, where an intense soliton

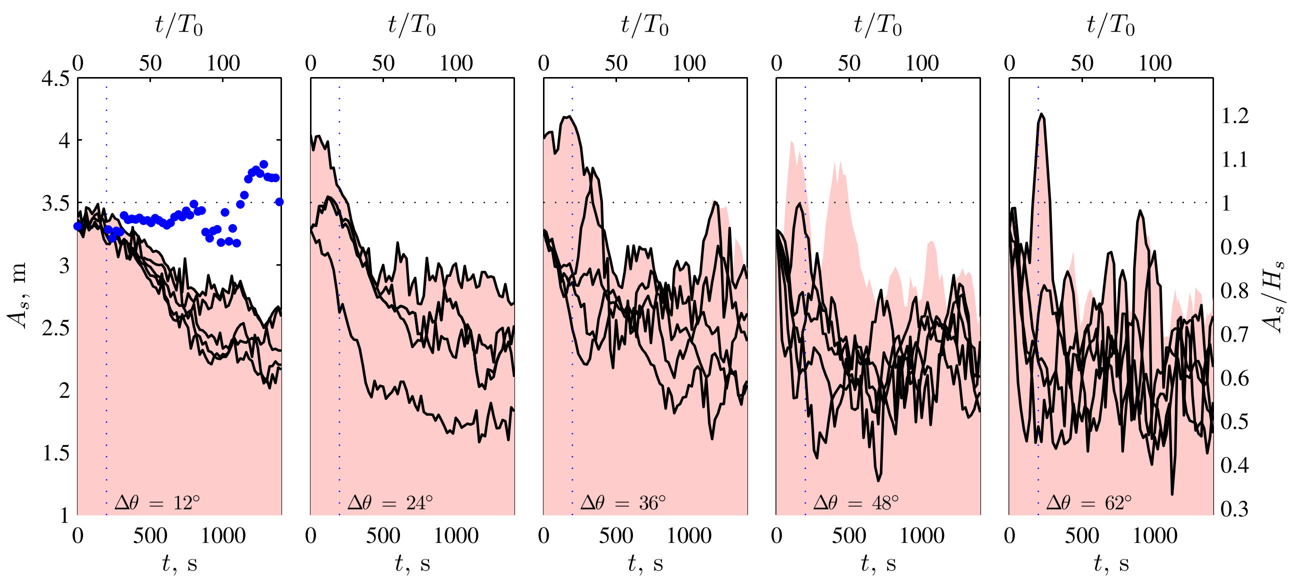

FIG. 8. Maximum soliton amplitudes for different situations of the directional spreading: in the selected region as shown in Figs. 6 and 7 (five black curves for different realizations) and in the entire simulated domain over all realizations (pink shadowed area). The maximum soliton amplitude in the unidirectional simulation[30] is given by blue dots in the leftmost panel for the reference. The vertical dotted line corresponds to $t = 200$ s.

structure is expected to appear. For broader angular spectra, intense solitons can emerge in different places, since the shaded areas in the plots are often located above the black curves.

As expected, the characteristic lifetime of intense soliton-like patterns is maximum in situations of long-crested waves. At large times, the maximum soliton amplitudes seem to stay at approximately the same level about $0.6\ldots0.7H_s$ in all cases. Under conditions of a relatively narrow angular spectrum, the maximum soliton amplitude decays to the background level within a few dozens of wave periods, whereas under short-crested wave conditions, the characteristic lifetime of soliton-like structures is just a few wave periods. It is interesting to note that in the simulations of short-crested waves, the momentary amplitudes of discovered "solitons" can be significantly higher than the value of H_s for a short time.

Thus, it can be concluded that long-lived nonlinear wave groups similar to envelope solitons of the NLSE can be detected in directional wave fields if the width of the angular spectrum is not too large. Section VI is dedicated to answering the question of how these soliton structures affect the statistical properties of surface waves.

VI. STATISTICAL FEATURES OF WAVE PATTERNS CONTAINING SOLITON-LIKE GROUPS

Several snapshots of the evolving water surface are shown in Fig. 9 in the comoving reference frame for the case $\Delta\theta = 12^\circ$ when a sustained soliton-like pattern is generated. Regions where the intense soliton is detected are accentuated by red dashed curves (same as the green circles in Fig. 6). In the selected areas, an intense group of waves can be discerned at all times. However, other intense wave groups may be seen in these examples of surfaces as well, which were not recognized as envelope solitons. Therefore, the influence of wave structures containing envelope solitons on the properties of the wave field as a whole is not obvious.

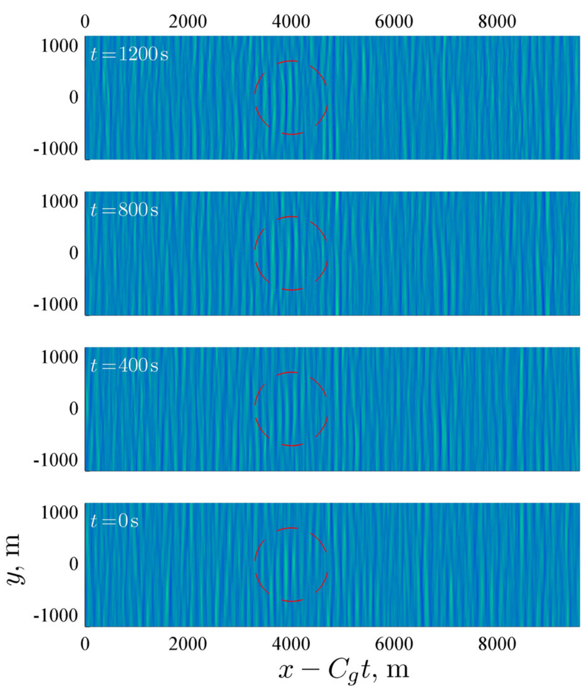

FIG. 9. Simulated surfaces of long-crested waves $\Delta\theta = 12^\circ$ in a comoving reference frame. The area where an intense soliton-like wave group is detected given by (12) is marked with the red dashed line.

In order to test if the presence of soliton-like structures modifies statistics of the simulated wave fields, we consider separately the areas where intense solitons are found with the help of the WIST, and the regions free of solitons. The selection of areas occupied by intense solitons is performed similar to the construction of the soliton function $A(x, y, t)$ but using a box-shaped generating function,

$$S(x, y = d_n, t = t_m) = \max_{A_s > H_s/2} H(w(A_s, k_s) - |x - x_s|). \qquad (14)$$

Here, $H(\cdot)$ denotes the Heaviside function, which returns 1 if its argument is positive and 0 otherwise. The maximum is taken over all revealed solitons with amplitudes exceeding half the significant wave height. According to Fig. 5, this amplitude condition selects 15%–25% of the most intense (and most localized) soliton-like groups. The mask width w is calculated according to Eq. (9) for the corresponding soliton parameters (A_s, k_s) and $W = 2$, and, thus, narrower adjacent regions than before are associated with solitons, see the blue line in Fig. 2. Finally, the sparsely defined function S is interpolated to the finer grid of the displacement $\eta(x, y, t)$ and is used to divide the water surfaces in two parts, labeled hereafter as the "soliton" data and "other waves."

Four statistical moments are computed for the "soliton" and remaining parts of the surface independently, and also for the original (unparted) surface according to the following formulas:

$$\bar{\eta}(t) = \langle \eta \rangle, \quad \sigma^2(t) = \langle (\eta - \bar{\eta})^2 \rangle,$$
$$\mu_3(t) = \frac{1}{\sigma^3} \langle (\eta - \bar{\eta})^3 \rangle, \quad \mu_4(t) = \frac{1}{\sigma^4} \langle (\eta - \bar{\eta})^4 \rangle, \qquad (15)$$

where the angle brackets denote averaging over the space (x, y), the time span of two dominant wave periods, $2T_p$, and the ensemble of five simulations. The obtained statistical moments for different conditions of the directional spreading are shown in Fig. 10.

According to graphs for the normalized second statistical moment σ (see the top row of Fig. 10), the areas associated with solitons are characterized by larger on average surface perturbations, which is most significant for narrower angular spectra and is almost absent for broad spectra with $\Delta\theta \geq 48^\circ$. Thus, long-lived soliton-like structures are found in regions characterized by locally enhanced wave amplitudes.

The curves of skewness μ_3 in the middle row of Fig. 10 do not exhibit any difference between the areas with solitons and free of them. The skewness starts from about zero at $t = 0$ and reaches an approximately equilibrium value at $t = 200$ s (see the vertical dotted lines) when nonlinearity of the code becomes fully effective. The curves for "solitons" are noisier obviously because of a smaller amount of data. It is interesting to note that in the simulations with different spreading parameters, the portion of the surface area associated with solitons does not demonstrate a noticeable dependence on $\Delta\theta$; in all cases, it is 5%–15%.

The fourth statistical moment of the surface displacement, kurtosis μ_4, is often used as an indicator of the ratio of the probabilities of waves with moderate and extreme amplitudes. For a normal (Gaussian) random process, the kurtosis is exactly 3. A larger value of kurtosis means a greater probability of extreme disturbances, a smaller

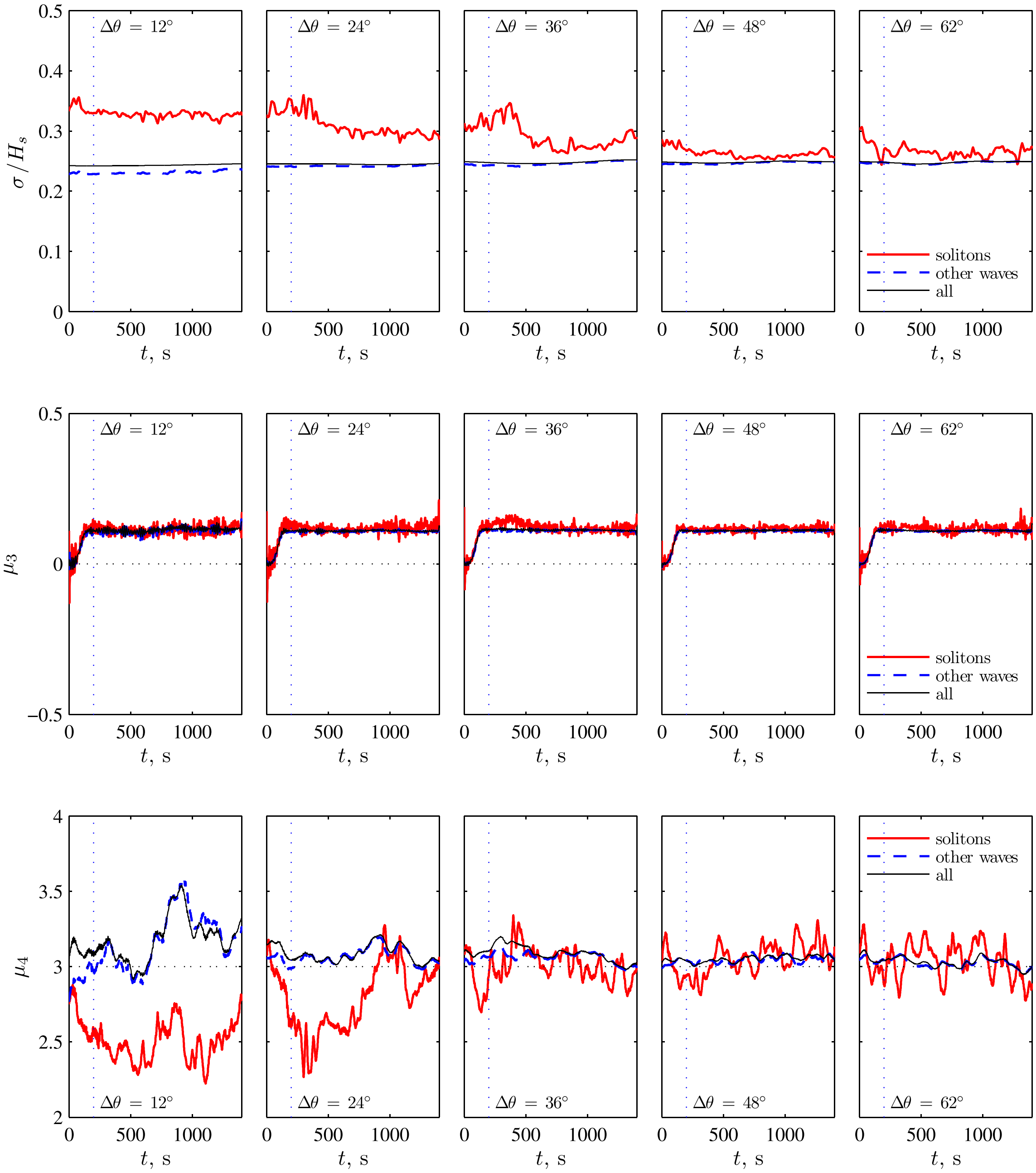

FIG. 10. Evolution of statistical moments of the surface displacement in the areas associated with envelope solitons, other waves, and all together: the root mean square displacement vs significant wave height (top), the skewness (middle), and kurtosis (bottom). The vertical dotted line corresponds to $t = 200$ s.

value—a lower probability of large perturbations. The graphs in the bottom row of Fig. 10 clearly show that the surface associated with soliton-like structures under conditions of a relatively narrow angular spectrum $\Delta\theta < 36°$ is characterized by a kurtosis noticeably less than 3. At the same time, the kurtosis of "other waves" as well as of the entire surface may become noticeably greater than 3 when waves are long-crested ($\Delta\theta = 12°$), which is consistent with the generally accepted understanding.[8,56] For a broad directional spreading $\Delta\theta \geq 36°$, the values of μ_4 in the areas occupied by "solitons" and ordinary waves are similar.

A dedicated study has revealed that the decrease in μ_4 for soliton patterns is caused by the growth of σ in these regions. If, in the formula (15), for μ_4, the value of σ in the denominator is replaced by the value characterizing the entire surface, then under conditions of a small scatter of wave directions, the kurtosis of the "soliton" areas will exceed the value of 3 several times. Therefore, if the local wave enhancement is not taken into account, waves in the areas associated with solitons will exhibit extreme probabilistic properties against the general background.

VII. CONCLUSIONS

In this work, we present the first example (to the best of our knowledge) of using the Inverse Scattering Transform to analyze directional water waves. The research is focused on the spectral conditions typical of the open ocean. Though storm waves often violate the assumptions of weak nonlinearity, narrow spectrum and planar geometry implied by the framework of integrable nonlinear Schrödinger equation, the idea of using the NLSE and its exact solutions to interpret sea wave data is quite popular in recent literatures, see, e.g., Refs. 10, 21, 22, 24, 25, 31, 36, and 39 among many others. It has received some support from laboratory experiments, in which the key examples of the nonlinear waves dynamics described by the NLSE were reproduced with reasonable accuracy. The windowed IST procedure employed in the present work has previously been tested within the Euler equations using examples of solitary groups[50] and irregular planar waves characterized by the JONSWAP spectrum.[30]

A well-defined group structure of deep-water oceanic waves and especially registrations of rogue events represented by sequences of very large waves further motivate interest in possible long-lived nonlinear solitary wave groups. If such stable groups can be recognized in stochastic sea wave fields, this could become an element of a short-term forecast of dangerous waves. Indeed, it has been shown in computational experiments that rogue wave events last longer under conditions suitable for the Benjamin–Feir instability and the related process of forming envelope solitons.[57,58] It is well known that under varying conditions (such as local depth and currents, external pumping or dissipation, etc.), linear waves and solitons behave very differently. At the same time, most of the experimental results refer to conditions of a single point measurement or/and planar waves. These restrictions are removed in the present work based on the direct numerical simulation of the primitive hydrodynamic equations.

Investigation of the soliton content in irregular waves with a prescribed spread of propagation directions is the main objective of the present work. For the study, we consider particular realizations of irregular JONSWAP waves, which, in the limit of strictly paraxial propagation, generate a long-lived soliton-type intense wave group.[30,44] It follows from the research that under conditions of moderate directional spreading, $\Delta\theta \lesssim 30^\circ$ envelope solitons with amplitudes of the order of the significant wave height $4\eta_{rms}$ may be continuously detected for a few tens of wave periods. The decay of intense soliton amplitudes occurs very similar in different realizations of the random transverse wave structure in the long-crested case $\Delta\theta = 12^\circ$ but is diverse when $\Delta\theta \geq 24^\circ$.

Envelope solitons may be detected in irregular wave fields under conditions of broader angular spectra too; their amplitudes can reach the significant wave height or even exceed it. However, these groups, which may resemble envelope solitons by the shape, are, in fact, transient; they quickly emerge and dissolve. Therefore, the fact that an envelope soliton is detected using the IST-based method in the field of short-crested waves does not itself mean either that a long-lived nonlinear wave group is found or that the wave conditions are suitable for the generation of envelope solitons or the modulational instability. At the same time, in the case of relatively long-crested waves, this may be considered as a reliable indicator of a presence of a soliton-type structure.

Soliton-like structures in wave fields with relatively narrow angular spectra are detected in "energy spots" of the water surface, which are characterized by a locally increased value of the average wave height. This circumstance is related to a paradoxical result that the soliton-like wave patterns are characterized by locally smaller values of the fourth statistical moment (kurtosis) of the surface displacement. At the same time, the kurtosis of the water surface occupied by detected solitons exhibits extreme values if the significant wave height of the entire wave field is used as the reference.

ACKNOWLEDGMENTS

The support of the laboratory of nonlinear hydrophysics and natural hazards of V.I. Il'ichev Pacific Oceanological Institute, Far Eastern Branch Russian Academy of Sciences, project of Ministry of Science and Education of Russia, Agreement No. 075-15-2022-1127 from July 1, 2022, and the support from the Foundation for the Advancement of Theoretical Physics and Mathematics "BASIS," Project No. 22-1-2-42, are gratefully acknowledged. The research was also partly supported by the Basic Research Program at the National Research University Higher School of Economics.

AUTHOR DECLARATIONS

Conflict of Interest

The authors have no conflicts to disclose.

Author Contributions

A. V. Slunyaev: Investigation (equal).

DATA AVAILABILITY

The data that support the findings of this study are available from the corresponding author upon reasonable request.

REFERENCES

1. V. Zakharov, "Statistical theory of gravity and capillary waves on the surface of a finite-depth fluid," Eur. J. Mech.-B/Fluids **18**, 327–344 (1999).
2. P. Janssen, *The Interaction of Surface Waves and Wind* (Cambridge University Press, 2004).
3. C. Kharif, E. Pelinovsky, and A. Slunyaev, *Rogue Waves in the Ocean* (Springer-Verlag, Berlin, Heidelberg, 2009).
4. M. Onorato, A. Osborne, M. Serio, and S. Bertone, "Freak waves in random oceanic sea states," Phys. Rev. Lett. **86**, 5831–5834 (2001).
5. M. Onorato, S. Residori, U. Bortolozzo, A. Montina, and F. Arecchi, "Rogue waves and their generating mechanisms in different physical contexts," Phys. Rep. **528**, 47–89 (2013).
6. P. Janssen, "Nonlinear four-wave interactions and freak waves," J. Phys. Oceanogr. **33**, 863–884 (2003).
7. N. Mori and P. Janssen, "On kurtosis and occurrence probability of freak waves," J. Phys. Oceanogr. **36**, 1471–1483 (2006).
8. M. Onorato, T. Waseda, A. Toffoli, L. Cavaleri, O. Gramstad, P. Janssen, T. Kinoshita, J. Monbaliu, N. Mori, A. Osborne, M. Serio, C. Stansberg, H. Tamura, and K. Trulsen, "Statistical properties of directional ocean waves: The role of the modulational instability in the formation of extreme events," Phys. Rev. Lett. **102**, 114502 (2009).
9. L. Shemer and A. Sergeeva, "An experimental study of spatial evolution of statistical parameters in a unidirectional narrow-banded random wavefield," J. Geophys. Res. **114**, C01015, https://doi.org/10.1029/2008JC005077 (2009).

[10]L. Shemer, A. Sergeeva, and A. Slunyaev, "Applicability of envelope model equations for simulation of narrow-spectrum unidirectional random field evolution: Experimental validation," Phys. Fluids **22**, 016601 (2010).
[11]M. Onorato, D. Proment, G. El, S. Randoux, and P. Suret, "On the origin of heavy-tail statistics in equations of the nonlinear Schrödinger type," Phys. Lett. A **380**, 3173–3177 (2016).
[12]A. Slunyaev, D. Pelinovsky, and E. Pelinovsky, "Rogue waves in the sea: Observations, physics, and mathematics," Phys.-Usp. **66**, 148–172 (2023).
[13]M. Christou and K. Ewans, "Field measurements of rogue water waves," J. Phys. Oceanogr. **44**, 2317–2335 (2014).
[14]F. Fedele, J. Brennan, S. de Leon, J. Dudley, and F. Dias, "Real world ocean rogue waves explained without the modulational instability," Sci. Rep. **6**, 27715 (2016).
[15]C. Kirezci, A. Babanin, and D. Chalikov, "Probabilistic assessment of rogue wave occurrence in directional wave fields," Ocean Dyn. **71**, 1141–1166 (2021).
[16]I. Teutsch and R. Weisse, "Rogue waves in the southern North Sea – the role of modulational instability," J. Phys. Oceanogr. **53**, 269–286 (2023).
[17]C. Mei, M. Stiassnie, and D.-P. Yue, *Theory and Applications of Ocean Surface Waves* (World Scientific, 2005).
[18]V. Zakharov, "Stability of periodic waves of finite amplitude on a surface of deep fluid," J. Appl. Mech. Tech. Phys. **9**, 190–194 (1968).
[19]V. Zakharov and A. Shabat, "Exact theory of two-dimensional self-focussing and one-dimensional self-modulation of waves in nonlinear media," Sov. Phys. - JETP **34**, 62–69 (1972).
[20]A. Osborne, *Nonlinear Ocean Waves and the Inverse Scattering Transform* (Academic Press, 2010).
[21]A. Chabchoub, N. Hoffmann, and N. Akhmediev, "Rogue wave observation in a water wave tank," Phys. Rev. Lett. **106**, 204502 (2011).
[22]A. Slunyaev, E. Pelinovsky, A. Sergeeva, A. Chabchoub, N. Hoffmann, M. Onorato, and N. Akhmediev, "Super rogue waves in simulations based on weakly nonlinear and fully nonlinear hydrodynamic equations," Phys. Rev. E **88**, 012909 (2013).
[23]A. Slunyaev and V. Shrira, "On the highest non-breaking wave in a group: Fully nonlinear water wave breathers vs weakly nonlinear theory," J. Fluid Mech. **735**, 203–248 (2013).
[24]J. Dudley, G. Genty, A. Mussot, A. Chabchoub, and F. Dias, "Rogue waves and analogies in optics and oceanography," Nat. Rev. Phys. **1**, 675–689 (2019).
[25]A. Chabchoub, A. Slunyaev, N. Hoffmann, F. Dias, B. Kibler, G. Genty, J. Dudley, and N. Akhmediev, "The Peregrine breather on the zero-background limit as the two-soliton degenerate solution: An experimental study," Front. Phys. **9**, 633549 (2021).
[26]Y. He, A. Slunyaev, N. Mori, and A. Chabchoub, "Experimental evidence of nonlinear focusing in standing water waves," Phys. Rev. Lett. **129**, 144502 (2022).
[27]N. Akhmediev and A. Ankiewicz, *Solitons: Nonlinear Pulses and Beams* (Chapman & Halls, 1997).
[28]A. Slunyaev, "Nonlinear analysis and simulations of measured freak wave time series," Eur. J. Mech.-B/Fluids **25**, 621–635 (2006).
[29]J. Soto-Crespo, N. Devine, and N. Akhmediev, "Integrable turbulence and rogue waves: Breathers or solitons?," Phys. Rev. Lett. **116**, 103901 (2016).
[30]A. Slunyaev, "Persistence of hydrodynamic envelope solitons: Detection and rogue wave occurrence," Phys. Fluids **33**, 036606 (2021).
[31]L. Fache, F. Bonnefoy, G. Ducrozet, F. Copie, F. Novkoski, G. Ricard, G. Roberti, E. Falcon, P. Suret, G. El, and S. Randoux, "Interaction of soliton gases in deep-water surface gravity waves," Phys. Rev. E **109**, 034207 (2024).
[32]W. Xia, Y. Ma, G. Dong, J. Zhang, and X. Ma, "Emergence of solitons from irregular waves in deep water," J. Mar. Sci. Eng. **9**, 1369 (2021).
[33]A. Gelash, S. Dremov, R. Mullyadzhanov, and D. Kachulin, "Bi-solitons on the surface of a deep fluid: An inverse scattering transform perspective based on perturbation theory," Phys. Rev. Lett. **132**, 133403 (2024).
[34]M. Onorato, L. Cavaleri, S. Randoux, P. Suret, M. Ruiz, M. de Alfonso, and A. Benetazzo, "Observation of a giant nonlinear wave-packet on the surface of the ocean," Sci. Rep. **11**, 23606 (2021).
[35]Y.-C. Lee, M. Bruhl, D.-J. Doong, and S. Wahls, "Nonlinear Fourier classification of 663 rogue waves measured in the Philippine Sea," PLoS One **19**, e0301709 (2024).
[36]A. Slunyaev, G. Clauss, M. Klein, and M. Onorato, "Simulations and experiments of short intense envelope solitons of surface water waves," Phys. Fluids **25**, 067105 (2013).
[37]A. Slunyaev, M. Klein, and G. Clauss, "Laboratory and numerical study of intense envelope solitons of water waves: Generation, reflection from a wall and collisions," Phys. Fluids **29**, 047103 (2017).
[38]P. Suret, A. Tikan, F. Bonnefoy, F. Copie, G. Ducrozet, A. Gelash, G. Prabhudesai, G. Michel, A. Cazaubiel, E. Falcon, G. El, and S. Randoux, "Nonlinear spectral synthesis of soliton gas in deep-water surface gravity waves," Phys. Rev. Lett. **125**, 264101 (2020).
[39]A. Chabchoub, K. Mozumi, N. Hoffmann, A. Babanin, A. Toffoli, J. Steer, T. van den Bremer, N. Akhmediev, M. Onorato, and T. Waseda, "Directional soliton and breather beams," Proc. Natl. Acad. Sci. U. S. A. **116**, 9759–9763 (2019).
[40]N. Mori, M. Onorato, and P. Janssen, "On the estimation of the kurtosis in directional sea states for freak wave forecasting," J. Phys. Oceanogr. **41**, 1484–1497 (2011).
[41]A. Kurkin and E. Pelinovsky, "Focusing of edge waves above a sloping beach," Eur. J. Mech.-B/Fluids **21**, 561–577 (2002).
[42]G. Wang, Q. Liang, F. Shi, and J. Zheng, "Analytical and numerical investigation of trapped ocean waves along a submerged ridge," J. Fluid Mech. **915**, A54 (2021).
[43]A. Slunyaev and V. Shrira, "Extreme dynamics of wave groups on jet currents," Phys. Fluids **35**, 126606 (2023).
[44]A. Slunyaev and A. Kokorina, "Soliton groups as the reason for extreme statistics of unidirectional sea waves," J. Ocean Eng. Mar. Energy **3**, 395–408 (2017).
[45]W. Xiao, Y. Liu, G. Wu, and D. Yue, "Rogue wave occurrence and dynamics by direct simulations of nonlinear wave-field evolution," J. Fluid Mech. **720**, 357–392 (2013).
[46]B. West, K. Brueckner, R. Janda, D. Milder, and R. Milton, "A new numerical method for surface hydrodynamics," J. Geophys. Res. **92**, 11803–11824, https://doi.org/10.1029/JC092iC11p11803 (1987).
[47]A. Slunyaev and A. Kokorina, "Numerical simulation of the sea surface rogue waves within the framework of the potential Euler equations," Izv., Atmos. Oceanic Phys. **56**, 179–190 (2020).
[48]A. Slunyaev and A. Kokorina, "Account of occasional wave breaking in numerical simulations of irregular water waves in the focus of the rogue wave problem," Water Waves **2**, 243–262 (2020).
[49]D. Dommermuth, "The initialization of nonlinear waves using an adjustment scheme," Wave Motion **32**, 307–317 (2000).
[50]A. Slunyaev, "Analysis of the nonlinear spectrum of intense sea waves with the purpose of extreme wave prediction," Radiophys. Quantum Electron. **61**, 1–21 (2018).
[51]V. Zakharov and A. Rubenchik, "Instability of waveguides and solitons in nonlinear media," Sov. Phys. - JETP **38**, 494–501 (1974).
[52]P. Drazin and R. Johnson, *Solitons: An Introduction* (Cambridge University Press, 1996).
[53]R. Mullyadzhanov and A. Gelash, "Direct scattering transform of large wave packets," Opt. Lett. **44**, 5298–5301 (2019).
[54]I. Mullyadzhanov, A. Gudko, R. Mullyadzhanov, and A. Gelash, "Numerical direct scattering transform for breathers," Proc. R. Soc. A **480**, 20230529 (2024).
[55]A. Slunyaev, E. Pelinovsky, and C. G. Soares, "Modeling freak waves from the North Sea," Appl. Ocean Res. **27**, 12–22 (2005).
[56]A. Slunyaev, "Effects of coherent dynamics of stochastic deep-water waves," Phys. Rev. E **101**, 062214 (2020).
[57]W. Fujimoto, T. Waseda, and A. Webb, "Impact of the four-wave quasi-resonance on freak wave shapes in the ocean," Ocean Dyn. **69**, 101–121 (2019).
[58]A. Kokorina and A. Slunyaev, "Lifetimes of rogue wave events in direct numerical simulations of deep-water irregular sea waves," Fluids **4**, 70 (2019).